Author/s:
Pan, S;Goudeli, E;Chen, J;Lin, Z;Zhong, QZ;Zhang, W;Yu, H;Guo, R;Richardson, JJ;Caruso, F

Title:
Exploiting Supramolecular Dynamics in Metal–Phenolic Networks to Generate Metal–Oxide and Metal–Carbon Networks

Date:
2021-06-21

Citation:
Pan, S., Goudeli, E., Chen, J., Lin, Z., Zhong, Q. Z., Zhang, W., Yu, H., Guo, R., Richardson, J. J. & Caruso, F. (2021). Exploiting Supramolecular Dynamics in Metal–Phenolic Networks to Generate Metal–Oxide and Metal–Carbon Networks. Angewandte Chemie International Edition, 60 (26), pp.14586-14594. https://doi.org/10.1002/anie.202103044.

Persistent Link:
https://hdl.handle.net/11343/274836

RESEARCH ARTICLE

Exploiting Supramolecular Dynamics in Metal–Phenolic Networks to Generate Metal–Oxide and Metal–Carbon Networks

Shuaijun Pan,[a] Eirini Goudeli,[b] Jingqu Chen,[a] Zhixing Lin,[a] Qi-Zhi Zhong,[a] Wenjie Zhang,[a] Haitao Yu,[a] Rui Guo,[+a] Joseph J. Richardson,[a] and Frank Caruso*[a]

[a] Dr. S. Pan, J. Chen, Z. Lin, Q.-Z. Zhong, Dr. W. Zhang, Dr. H. Yu, R. Guo,[+] Dr. J. J. Richardson, and Prof. F. Caruso
ARC Centre of Excellence in Convergent Bio-Nano Science and Technology, and the Department of Chemical Engineering
The University of Melbourne
Parkville, Victoria 3010, Australia
E-mail: fcaruso@unimelb.edu.au

[b] Dr. E. Goudeli
Department of Chemical Engineering
The University of Melbourne
Parkville, Victoria 3010, Australia

[+] Present address:
State Key Laboratory of Chemo/Biosensing and Chemometrics, and College of Chemistry and Chemical Engineering
Hunan University
Changsha 410082, China

Supporting information for this article is given via a link at the end of the document.

Abstract: Supramolecular complexation is a powerful strategy for engineering materials in bulk and at interfaces. Metal–phenolic networks (MPNs), which are assembled through supramolecular complexes, have emerged as suitable candidates for surface and particle engineering owing to their diverse properties. Herein, we examine the supramolecular dynamics of MPNs during thermal transformation processes. Changes in the local supramolecular network including enlarged pores, ordered aromatic packing, and metal relocation arise from thermal treatment in air or an inert atmosphere, enabling the engineering of metal–oxide networks (MONs) and metal–carbon networks, respectively. Furthermore, by integrating stimuli-responsive motifs, the MONs are endowed with reversible superhydrophobic (>150°) and superhydrophilic (~0°) properties. By highlighting the thermodynamics of MPNs and their transformation into diverse materials, this work offers a versatile pathway for advanced materials engineering.

Introduction

Nanostructured composite materials and thin films with controlled physicochemical properties have found applications in diverse fields, including bioproduction,[1] surface and particle engineering,[2] energy and photocatalysis,[3] self-cleaning,[4] and bio–nano interactions and biomedical applications.[5] Advances in metal–organic nanocomposite materials have been driven by in-depth mechanistic understandings of their design principles.[6] Supramolecular complexation, through the integration of discrete motifs via diverse intermolecular forces, allows for the engineering of functional nanocomposite materials.[6d,7] Metal coordination with organic ligands allows for the engineering of functional and tailorable organic–inorganic supramolecular complexes both in bulk as particles[5b,8] and at interfaces as coating materials.[2a,9] Specifically, metal–phenolic networks (MPNs)[2a] represent an emerging platform for coating and functionalizing diverse substrates by combining the advantages of metal coordination and the various interfacial interactions displayed by polyphenols.[6b,10] The dynamic nature of coordination bonding in MPNs enables the engineering of responsive interfaces with controlled interfacial properties;[2a] however, their supramolecular dynamics remain largely unexplored, especially in regards to thermodynamic structures.[6a] Supramolecular network transformations provide insight into network dynamics, allowing the tuning of material properties, and are fundamental for precise molecular engineering and surface engineering.[11] Investigating the thermal behavior of supramolecular structures in MPNs is, therefore, fundamental for the development of MPN-derived functional composite materials.[2d,9b,12]

In the present work, the dynamics of MPN supramolecular complexes was investigated both computationally and experimentally in oxidative (air) or inert (argon) atmospheres at different temperatures (**Figure 1**). Thin films of MPNs were first formed on sacrificial templates ($CaCO_3$) through the one-pot assembly of metal ions (e.g., Fe^{III}) and a multidentate phenolic ligand (i.e., tannic acid, TA) (**Figure S1**), which can transform into metal–carbon networks (MCNs) or metal–oxide networks (MONs) upon heating under inert or oxidative conditions, respectively (**Figure 1a**). Capsules were obtained after template removal, and the thickness of these hollow structures was tuned by the number of coating steps. The present study is largely focused on hollow structures as they provide insight into free-standing networks through characterization methods that are not readily applicable to bulk complexes and coatings on planar substrates. Furthermore, hollow structures are promising in diverse fields including energy harvesting[13] and drug delivery.[14] Thin films are also examined to demonstrate switchable wetting. Thermal transitions of the amorphous MPNs resulted in the formation of more highly ordered composite networks, where crystalline structures were observed. Other changes, including network porosity, inter-species spacing, and π–π stacking, were investigated both experimentally and computationally. Finally, the

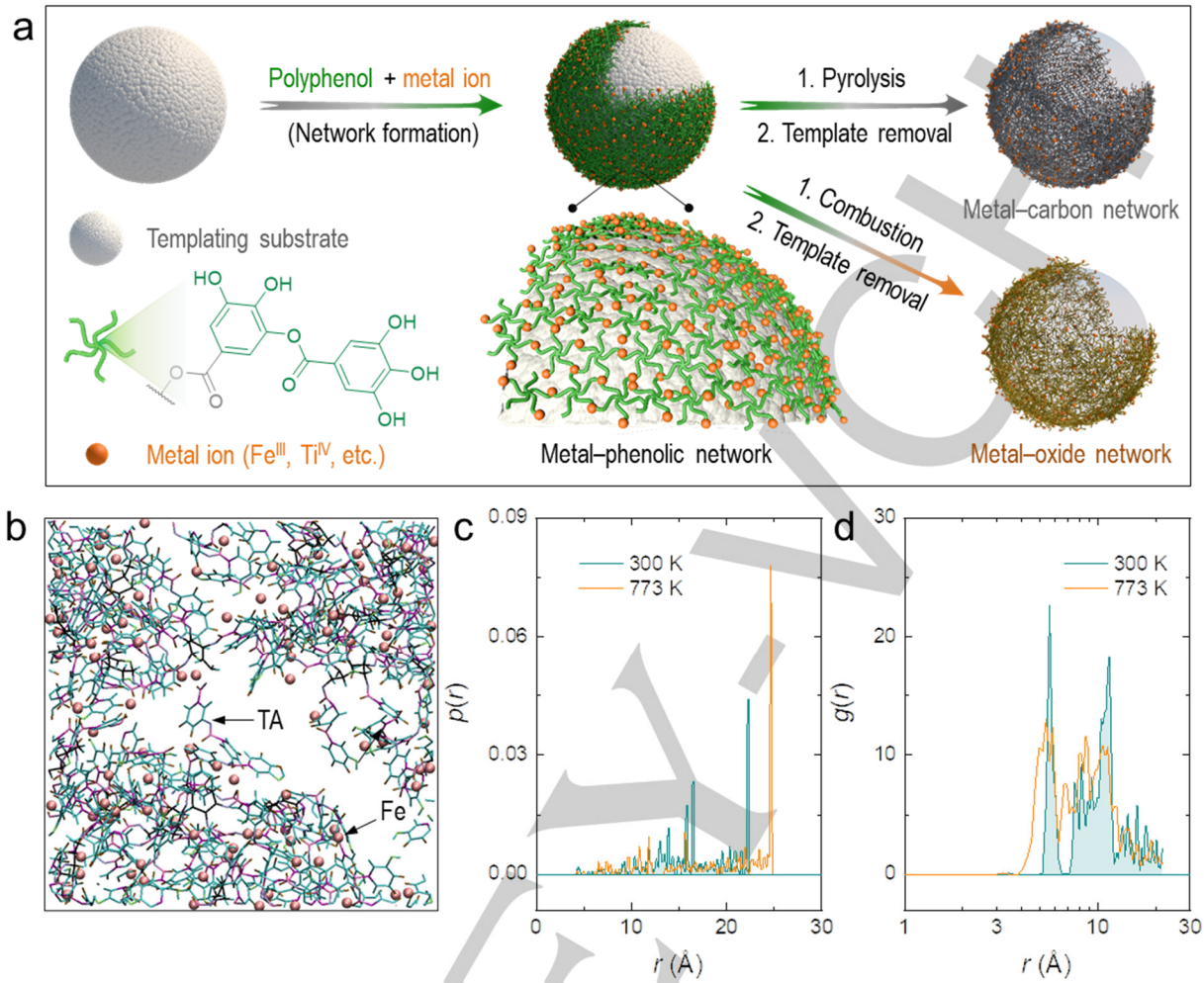

Figure 1. Design of nanoporous metal–oxide and metal–carbon networks via heat transformation of MPNs. (a) Schematic of the preparation of MPN and its transformation to MON and MCN upon heat treatment. (b) Representative configuration of MPN in the simulation cell studied. (c) Probability distribution function ($p(r)$) of pore size and (d) aromatic ring–ring radial distribution ($g(r)$) in MPNs upon heat treatment at different temperatures.

structural and configuration/composition transformations of MPNs allowed for the tuning of surface physicochemical properties, including reversible surface wettability.

Results and Discussion

To validate the occurrence of network transformations, we first investigated the molecular dynamics (MD) of MPNs at different temperatures by computing their supramolecular structures (**Figure 1b; Movies S1 and S2; see *Molecular Dynamics (MD) Simulations* in Supporting Information**). MPN clusters (i.e., Fe_5TA) were generated to represent the basic constitutional unit of MPNs. This metal-to-TA molar ratio (5:1) was chosen to represent the bis-complex formed when assembling MPNs based on ligand-to-metal charge transfer band studies of MPNs and MPN capsules (**Figures S2–S5**).[8a,9a] Upon application of heat to the model system, the MPNs underwent thermodynamic delocalization within confined space, mimicking the movement of the intercorrelated MPN clusters. Probability distribution curves of the MPN clusters revealed their different thermodynamic behaviors at the different temperatures examined, i.e., 300 K (room temperature) and 773 K (**Figure 1c**). The MPN clusters were largely found at a radial distance of ~22 Å at 300 K, which shifted to a larger value of ~25 Å at 773 K, indicating the potential of tuning local structures (e.g., porosity) of MPNs by heat.

In addition to providing insight into the thermodynamics of MPN building blocks, MD simulations revealed the aromatic ring–ring packing by the radial distribution function $g(r)$ (**Figure 1d**). At 300 K, the aromatic ring–ring packing featured two dominant interspacing values (i.e., ~6 and ~10 Å, corresponding to the positions of the first- and second-nearest ring neighbors), which are likely due to the bilayer structure of the aromatic rings that surround the glucose center of the TA molecule (**Figure S1**). Heating at 773 K could overcome the energy barrier of the network, leading to closer ring–ring packing (the first-nearest ring neighbors appeared at ~4 Å) and broadening of spacing features (**Figure 1d**). These observed features indicate the potential of generating ordered structures upon heating amorphous MPNs.

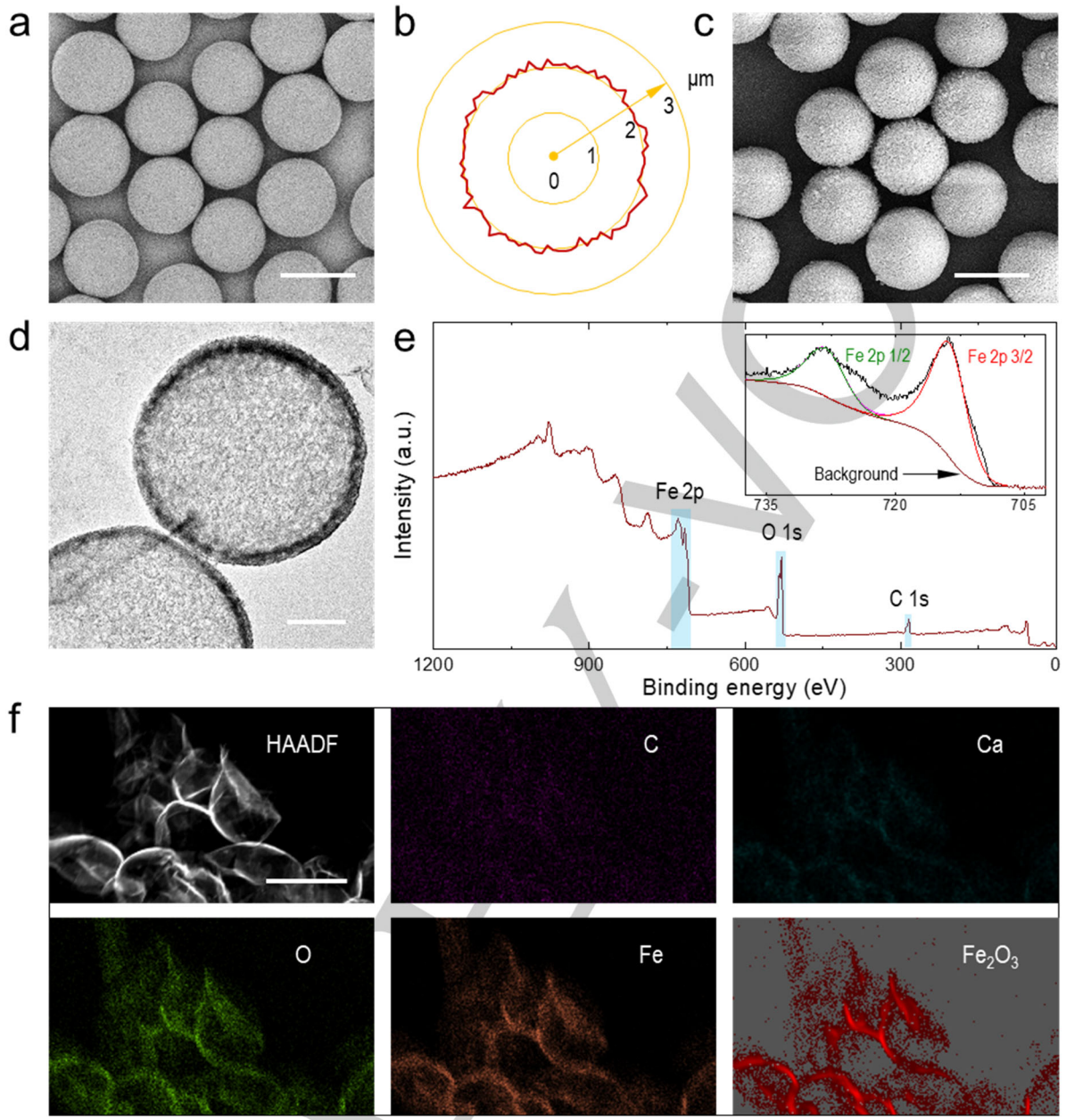

Figure 2. MONs. (a) Scanning electron microcopy (SEM) image of $CaCO_3$ template particles and (b) radar map of their size distribution (100 particles); scale bar is 2 μm. (c) SEM image of $CaCO_3$@MON; scale bar is 2 μm. (d) TEM image of Fe_2O_3 (MON) capsules (prepared from 3 MPN layers); scale bar is 500 nm. (e) XPS survey map of Fe_2O_3 capsules. Inset is the high-resolution XPS spectrum of Fe 2p. (f) High-angle annular dark-field (HAADF) image and elemental mapping of Fe_2O_3 capsules (prepared from 1 MPN layer). A scale bar of 3 μm applies to all images in (f).

Besides these thermodynamic structural changes, the configurations of the basic building blocks were mostly unchanged, as observed from the radial distribution functions of Fe–TA, Fe–Fe, and TA–TA (**Figure S6**). The thermal stability of the MPNs was also experimentally investigated by thermal gravimetric analysis (TGA) in argon (**Figure S7**). A steep weight loss occurred at ~973 K (700 °C), likely owing to the breakdown of metal–phenol bonds (thereby loss of organic moieties), whereas a slower weight loss was observed at ~773 K (500 °C), likely due to volatile species generated by pyrolysis, indicating a largely preserved (and carbonized) structural network at ~773 K—a suitable temperature chosen for the controlled thermal transformations and MD simulation studies. These preliminary findings (i.e., MD simulations and TGA) of MPN thermodynamics provide a strategic basis for engineering advanced nanoporous structures.

To experimentally study the thermodynamic transformations of MPNs, monodisperse calcium carbonate ($CaCO_3$) template particles[9a] (D = 1.9 ± 0.1 μm) were synthesized (**Figure 2a and 2b**) and coated with MPNs via the addition of metal ions (e.g., Fe^{III}) and phenolic ligands (e.g., TA) (**Figure S8 and *Experimental Procedures* in Supporting Information**). For the heating process, 773 K was chosen based on the TGA study and

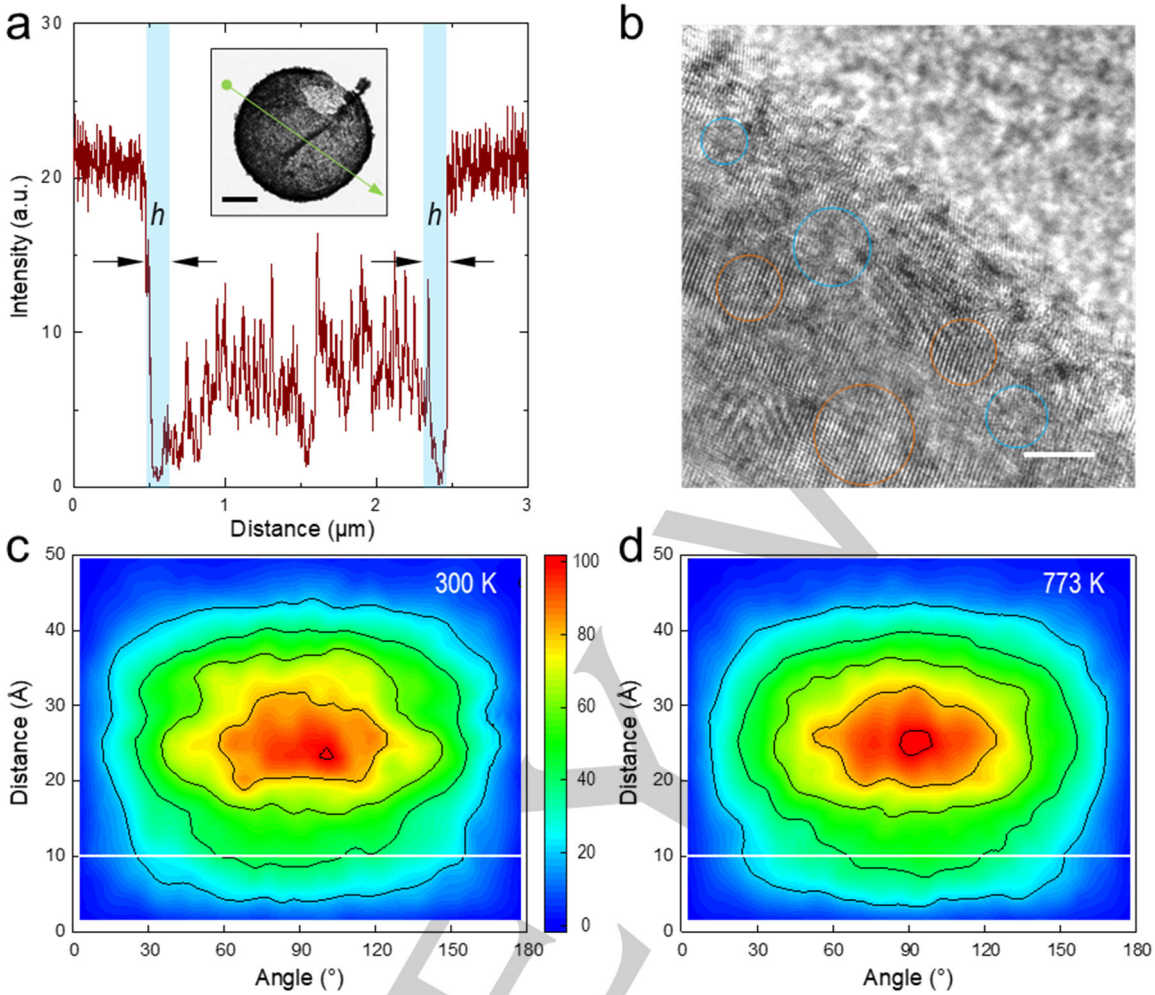

Figure 3. MCNs. (a) Thickness measurement of an MCN capsule. Inset is a representative TEM image; scale bar is 500 nm. (b) High-resolution TEM image of an MCN showing the presence of amorphous (blue) and lattice (orange) structures; scale bar is 5 nm. (c, d) Two-dimensional (2D) contour images (averaged) of aromatic ring–ring distance (between the mass centers of all possible pairs of rings) versus ring–ring stacking angle within MPNs at 300 K (c) and 773 K (d) based on MD simulations. The black lines correspond to color levels (i.e., event counts) of 20, 40, 60, 80, and 100, from outer to inner, respectively. The white lines are for reference.

the MD simulations and because $CaCO_3$ is stable at that temperature (i.e., decomposition of $CaCO_3$ into CaO and CO_2 occurs at >873 K) (**Figure S9**). Thus, $CaCO_3$ can then be selectively and completely removed after heating via competitive calcium binding with ethylenediaminetetraacetic acid (EDTA) to form hollow structures (**Figure 2d**). The surface of the MPN-coated $CaCO_3$ particles displayed nanoporous features after heating in air at 773 K for 2 h to form MONs (**Figure 2c**). After core removal, X-ray photoelectron spectroscopy (XPS) survey spectra revealed the prevalent presence of Fe and O (intensity ratio of the core level XPS peaks was 1:1.5 Fe/O) and traces of C (<1 at.%) (**Figure 2e**). The multiplet split in the Fe 2p spectrum at 710–730 eV indicated the presence of a high-spin Fe^{III} compound, with characteristic satellite features of Fe 2p at binding energies of ~724 eV and ~711 eV, which collectively confirmed the oxidation state of Fe in the MON capsules (i.e., Fe_2O_3).[15] Energy-dispersive X-ray spectroscopy further confirmed the elemental distribution and elemental content of the resultant MON capsules (**Figure 2f**), which demonstrated that the purity of the Fe_2O_3 capsules was >99.4 at.% with negligible impurities of Ca and C (**Figure S10**). Additionally, the thickness of the MON capsules was easily tuned by the number of MPN deposition steps performed on the sacrificial $CaCO_3$ templates (**Figure S11**), where a 3-layered MON resulted in a free-standing hollow structure with a ~100 nm thick shell (**Figure S12**). Additionally, the MON capsules obtained from amorphous MPN coatings[16] possessed a more ordered nanostructure (e.g., hematite) when compared with MONs prepared from free MPN complexes (without template), as indicated by their respective X-ray powder diffraction spectra (**Figure S13**). This is likely due to the dominant bis-complex building units (rather than a mixture of mono-, bis-, and tris-complexes) in the MPNs and their confined structures (originating from the sacrificial template surface), whereas MONs produced from free MPN complexes have variable local nanoporous structures. A series of MON capsules were also engineered from MPNs containing other metal species (e.g., Ti^{IV}, Ce^{III}, Cr^{III}, and Zr^{IV} **Figure S14**) owing to the strong binding of TA to transitional metals[9a] (**Figure S15**).

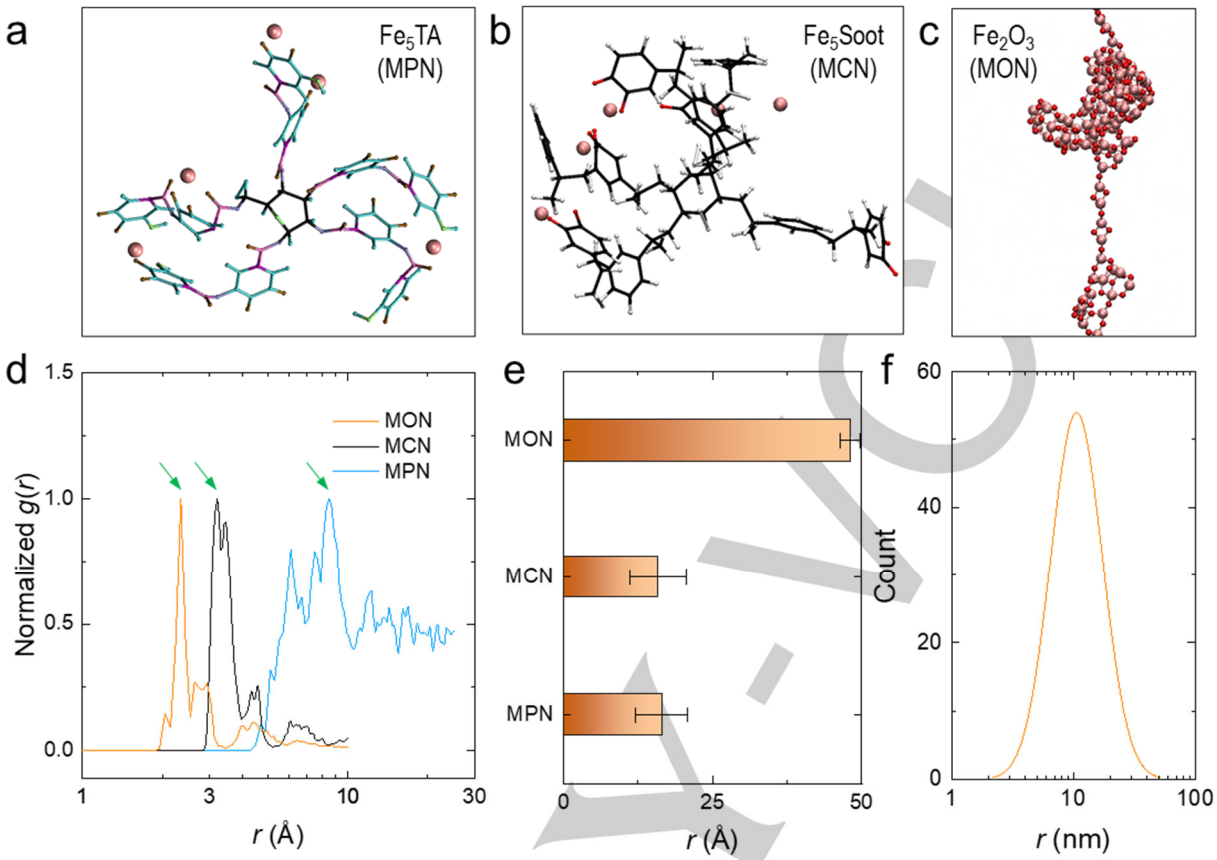

Figure 4. MD simulations of MPN, MCN, and MON systems. (a) Representative conformation of an MPN cluster. (b) Subunit of MCN represented by an oxidized soot particle. (c) Simulated MON structure. (d) Normalized Fe–Fe radial distributions in MPN, MCN, and MON. Arrows indicate the dominant Fe–Fe spacing. (e) Simulated average pore (radial) sizes in MPN, MCN, and MON. Error bars are standard deviations of 2000 measurements performed at a radial distance step of 0.05 Å in the range of 0–100 Å. (f) Experimentally measured pore size distribution of MON nanoporous structures based on >300 nanopores.

The thermodynamic transformation of MPNs was also studied at 773 K in argon. The inert atmosphere enabled the conservation of carbon species, leading to the formation of MCNs on the surface of $CaCO_3$ (**Figure S16**). MCN capsules with a shell thickness of ~100 nm were obtained after $CaCO_3$ removal with EDTA (**Figure 3a**, **Figure S17**). High-resolution transmission electron microscopy (TEM) images revealed that both amorphous and ordered lattice structures were present in the MCN capsules (**Figure 3b**). The interspacing of the lattice structures was determined to be ~3.4 Å, indicating the formation of graphitized carbon networks resulting from the thermodynamic reorganization of MPN building blocks at elevated temperatures[17] (**Figure S18**). The interspacing of the graphitic lattice features determined experimentally was consistent with the simulation results in **Figure 1d**, which indicated that the shortest distance between adjacent aromatic rings was 4–6 Å at 773 K. This finding confirms the feasibility of molecular design and engineering of highly ordered materials from amorphous MPNs.

To better understand the resultant local stacking structures in MCNs, the ring–ring distance and ring–ring angle were determined by MD simulations of MPN thermodynamics over 0.10–0.45 ns at 300 K (**Figure S19**) and 773 K (**Figure S20**). The average angle between aromatic rings was 90.1° (with a standard deviation of 39.5°) at 300 K and the average (center–center) ring–ring distance was 25.0 ± 10.4 Å (**Figure 3c**). Upon heat treatment at 773 K, the ring–ring stacking features changed minimally, with average distance and angle of 24.5 ± 10.3 Å and 89.8 ± 39.3°, respectively (**Figure 3d**). However, the ring–ring distances decreased considerably (i.e., <10 Å) and a higher fraction of adjacent rings at roughly perpendicular angles to each other were observed at the higher temperature (i.e., 773 K) (**Figure S21**). For comparison, the ring–ring stacking in MCNs using iron soot (Fe_5Soot) was simulated (**Figures S22–S24**). Likewise, the rings largely packed to an angle of ~90° but at a closer distance of ~20 Å owing to the mass loss during pyrolysis. These results demonstrate the transformation of amorphous films into more ordered and functional metal–carbon nanostructures.[8d,18]

Along with the thermodynamic transformation and network reorganization, the surface properties of the MPN-coated substrate changed after heat treatment (**Figure S25**). The deposition of MPNs onto $CaCO_3$ led to an overall negative zeta potential, shifting from –26 mV before coating to –47 mV after coating. Removal of carbonaceous species to form MONs led to a slightly less negative zeta potential (–15 mV). Decomposition of the phenolic motifs during the carbonization process in argon to form MCNs led to a positive zeta potential (20 mV). These results

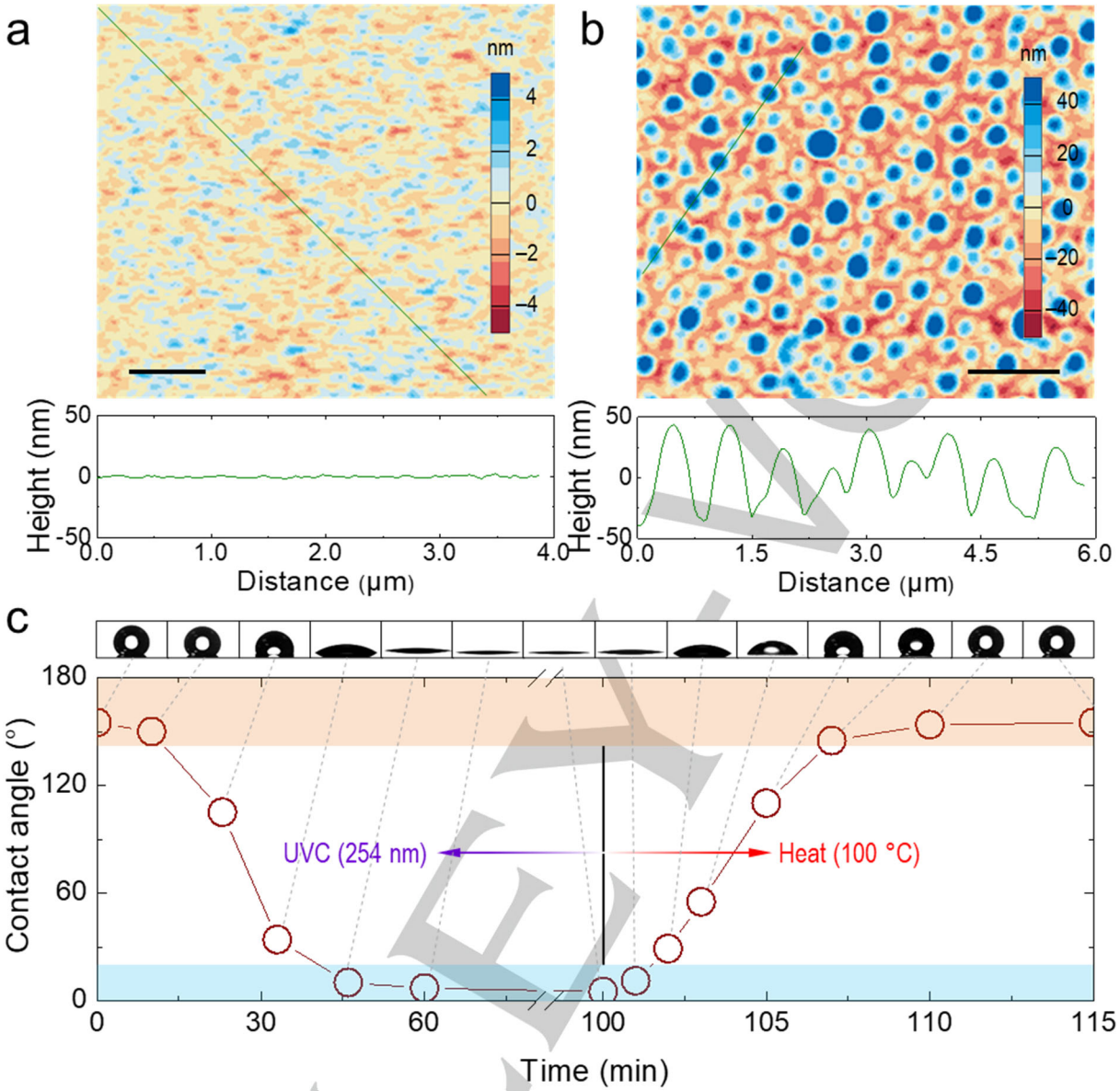

Figure 5. Thermo-initiated thin film dewetting and photo-induced switchable surface wettability. (a) Atomic force microscopy (AFM) image and line profile of a Ti^{IV} MPN coated on a planar silicon substrate; scale bar is 500 nm. (b) AFM image and line profile of TiO_2 after heat-conversion of Ti^{IV} MPN; scale bar is 2 μm. (c) Wettability of the silane-modified TiO_2 surface and its dual responsiveness to UVC light and heat treatment.

show that the surface properties can be reversibly switched by repeating the MPN deposition and thermal decomposition process in air or inert conditions[7b] (**Figure S26**). Additionally, the permeability of the MPN, MCN, and MON capsules underwent considerable changes owing to the transformation of these networks. Confocal laser scanning microscopy showed that MPN capsules displayed a size-exclusion effect on fluorescein isothiocyanate-labeled dextran polymers (FITC–$dextran_{Mw}$) of varying average molecular weights (M_w = 4, 10, 70, 250, 500, and 2000 kDa) and thereby different hydrodynamic sizes (**Figure S27**). For example, the MPN capsules were highly permeable (>90%) to FITC–dextran with a smaller M_w and less permeable as the M_w increased to becoming impermeable to FITC–$dextran_{2000kDa}$, consistent with a previous report[2a] (**Figure S28**). In contrast, the heat-transformed networks (MCN and MON capsules) were highly permeable (>90%) to all FITC–dextran studied, indicating that the effective pore size (i.e., equivalent hydrodynamic size of the permeate) of the MCN and MON capsules was >50 nm in diameter.

We therefore computed and compared the local network organization of the different subunits (**Figure 4a–c**), which showed that the local density of the transformed networks varied considerably between the systems (**Figure S29**). For example, the metal species were distributed evenly (1.5 Fe per nm^3 on average) across the simulation cell of MCNs (**Movie S3**); however, after further removal of carbon species at elevated temperatures, the Fe_2O_3 clusters moved closer to each other and became aggregated (**Movie S4**) leaving most of the simulated cell empty (i.e., enlarged pore size). The metal components, which did not

decompose during heat treatment, were examined as well as their dynamics and distribution in the networks (**Figure 4d**). Fe–Fe radial distribution functions (normalized by their maximum value) of the three systems at 300 K revealed that the Fe–Fe distance gradually decreased as more organic components were removed upon heat treatment, with their first peaks (i.e., dominant) appearing at radial distances of 8.5, 3.2, and 2.3 Å for MPN, MCN, and MON, respectively. The thermodynamic reorganization of Fe–Fe led to the formation of local pores among their constituent units (**Figure 4e**), where MONs exhibited the largest pore size (average radial distance of 48.1 ± 1.7 Å). This value was >3-fold higher than the pore size of MPNs (16.5 ± 4.4 Å) based on the MD simulations. These simulated results explain the high permeability of the MON capsules. The pore size within MON capsules was also analyzed by TEM using both ImageJ analyzer (**Figure S30**) and Image Color Summarizer (**Figure S31**). The pore size distribution of MONs in **Figure 4f** indicates that the average radial pore size was 15 nm with a standard derivation of 8 nm, which is consistent with the value determined from the permeability studies. Despite the slight inconsistencies between the simulation data and experiments (owing to the smaller size of the simulation cell), the current design principle and study methods could serve as a reference for future nanopore design and analysis.[19] It is also noted that the pore features generated in MONs are in general larger than many metal–organic frameworks[6k,6l] or covalent organic frameworks[6m,6n] (e.g., <10 nm) but hold promise for tunable pore sizes by molecular engineering.

In addition to particle engineering, the thermal transformation of MPNs offers a route to control the macroscopic surface properties (e.g., wettability) of materials through changes in the local roughness.[20] A superhydrophilic (water contact angle <10°) microscopically smooth (root-mean-square (rms) roughness ~0.8 nm) conformal Ti-based MPN film was deposited on silicon wafers by mixing TA and Ti^{IV} (**Figure 5a, Figure S32**). After MPN-to-MON conversion at 773 K in air, the resulting silicon substrate became >20-fold rougher (**Figure 5b**; rms ~20 nm) with a thin layer (~40 nm) of discrete TiO_2 particles sparsely covering the substrate (**Figure S33**). The mechanism of TiO_2 particle formation (arising from the oxidative decomposition of the conformal MPN thin film) can be analyzed by its Voronoi diagram[21] (**Figure S34**). The relationship between the Voronoi area A_i and Feret diameter d_i of each particle i can be evaluated according to the mass balance equation (see details in **Figure S35**):

$$A_i \sim \frac{\rho_2}{\rho_1 \delta (1-\beta)} d_i^3$$

where δ and β are the initial thickness and coefficient of materials loss, respectively, and ρ_1 and ρ_2 are the density of MPN before and after thermal treatment. The linear relationship between A_i and d_i in logarithmic coordinates (**Figure S35**) indicated that the TiO_2 particles were produced as a result of MPN film contraction and subsequent oxidative transformation at 773 K. It is noted that the aforementioned Feret–area relationship can be used for tuning surface properties (e.g., particle size, roughness, and porosity) by controlling the parameters of the initial MPN thin films including thickness, composition, and metal–organic ratios, in addition to the phase transformation conditions (e.g., temperature, time, and gaseous media).

The surface wettability of the MON films could be tuned upon modification with a low-energy silane coupling agent. The resultant TiO_2 surfaces displayed super-repellency to water (contact angle >160°) with negligible contact angle hysteresis (i.e., roll-off angle <5°). Irradiation with ultraviolet light (UVC, 254 nm) for 60 min led to Ti–O bond rupture and the generation of surface oxygen vacancies,[22] and consequently complete surface wetting by water (**Figure 5c**). The super-repellency was restored by subsequent heat treatment at 100 °C for 10 min. The surface wettability was efficiently reversibly switched between superwetting and superhydrophobicity through at least seven UVC–heat treatment cycles (**Figure S36**) with negligible impact on the film morphology (**Figure S37**). Moreover, the converted superwetting can be maintained for a few days by avoiding heating and light exposure.[22c] Illumination with UVA (365 nm) for ~2 h did not cause significant wettability changes to the original super-repellent TiO_2 surface (**Figure S38**) but activated the super-repellency properties of the UVC-degraded TiO_2 surface owing to the reconstitution of Ti–O bonds and therefore reduced surface oxygen vacancies.[23] The intrinsic photocatalytic activities[24] of TiO_2, its photo-responsive wettability, in combination with the studied structural conversions suggest the potential applications of these materials in diverse fields including self-cleaning, photocatalysis, water treatment, and antifogging.

Conclusion

The thermal conversion of supramolecular MPNs was examined as a versatile platform for the engineering of nanoporous networks and functional surfaces. The supramolecular platform underwent selective transformations depending on the atmosphere used for heat treatment to form MONs (oxygen) and MCNs (argon). Upon thermodynamic transformation, the resultant networks featured locally increased ordered structures, an overall increase in network porosity and permeability, as well as changes in surface properties (e.g., zeta potential, roughness). When stimuli-responsive motifs (i.e., TiO_2) are combined with hydrophobic polymers, the resulting MONs displayed controlled and reversible wetting. The tailorable supramolecular MPN scaffolds, selective thermodynamic structural transformations, and access to a series of physicochemical properties of nanoporous materials demonstrated in this study have fundamental implications for energy and photocatalysis applications[3] and the advanced engineering of functional materials, e.g., metallosuperstructures,[6g] dynamics of complex systems,[25] energy generators,[26] micropollutant control,[27] bioresponsive carriers,[28] and architecture-transformable materials,[11b] and may promote advances in supramolecular assemblies.[29]

Acknowledgments

We thank Prof. W. Xu, Dr. M. A. Rahim, Dr. J. Zhou, Dr. Y. Ju, and Dr. X. Duan for helpful discussions and/or support with the characterization studies. This research was supported by the following grants, schemes, and fellowships: Australian Research Council Centre of Excellence in Convergent Bio-Nano Science and Technology (F.C., Project no. CE140100036), National Health and Medical Research Council Senior Principal Research Fellowship (F.C., GNT1135806). This work was performed in part at the Materials Characterisation and Fabrication Platform

(MCFP), the Bio21 Advanced Microscopy Facility, the Trace Analysis for Chemical, Earth and Environmental Sciences (TrACEES) Platform, and the Materials and Process Simulation (MAPS) platform at The University of Melbourne.

Keywords: microporous materials • reversible wettability • superhydrophobic surfaces • supramolecular chemistry • thermal transition

[1] J. Guo, M. Suástegui, K. K. Sakimoto, V. M. Moody, G. Xiao, D. G. Nocera, N. S. Joshi, *Science* **2018**, *362*, 813–816.

[2] a) H. Ejima, J. J. Richardson, K. Liang, J. P. Best, M. P. Van Koeverden, G. K. Such, J. Cui, F. Caruso, *Science* **2013**, *341*, 154–157; b) A. Levin, T. A. Hakala, L. Schnaider, G. J. L. Bernardes, E. Gazit, T. P. J. Knowles, *Nat. Rev. Chem.* **2020**, *4*, 615–634; c) H. Lee, S. M. Dellatore, W. M. Miller, P. B. Messersmith, *Science* **2007**, *318*, 426–430; d) M. Schöttle, Q. Xia, Y. T. Cheng, N. D. Shepherd, C. D. Ling, M. Müllner, *Chem. Mater.* **2020**, *32*, 4716–4723.

[3] a) C. Xu, P. Ravi Anusuyadevi, C. Aymonier, R. Luque, S. Marre, *Chem. Soc. Rev.* **2019**, *48*, 3868–3902; b) X. Lang, A. Hirata, T. Fujita, M. Chen, *Nat. Nanotechnol.* **2011**, *6*, 232–236.

[4] a) S. Pan, R. Guo, M. Björnmalm, J. J. Richardson, L. Li, C. Peng, N. Bertleff-Zieschang, W. Xu, J. Jiang, F. Caruso, *Nat. Mater.* **2018**, *17*, 1040–1047; b) M. Liu, S. Wang, L. Jiang, *Nat. Rev. Mater.* **2017**, *2*, 17036; c) S. Pan, R. Guo, J. J. Richardson, J. D. Berry, Q. A. Besford, M. Björnmalm, G. Yun, R. Wu, Z. Lin, Q.-Z. Zhong, J. Zhou, Q. Sun, J. Li, Y. Lu, Z. Dong, M. K. Banks, W. Xu, J. Jiang, L. Jiang, F. Caruso, *Adv. Sci.* **2019**, *6*, 1901846.

[5] a) J. Guo, Y. Ping, H. Ejima, K. Alt, M. Meissner, J. J. Richardson, Y. Yan, K. Peter, D. von Elverfeldt, C. E. Hagemeyer, F. Caruso, *Angew. Chem. Int. Ed.* **2014**, *53*, 5546–5551; *Angew. Chem.* **2014**, *126*, 5652–5657; b) M. Chen, C. Peng, Y. Su, X. Chen, Y. Zhang, Y. Wang, J. Peng, Q. Sun, X. Liu, W. Huang, *Angew. Chem. Int. Ed.* **2020**, *59*, 20988–20995; *Angew. Chem.* **2020**, *132*, 21174–21181.

[6] a) A. K. Cheetham, G. Kieslich, H. H. Yeung, *Acc. Chem. Res.* **2018**, *51*, 659–667; b) J. Zhou, Z. Lin, Y. Ju, M. A. Rahim, J. J. Richardson, F. Caruso, *Acc. Chem. Res.* **2020**, *53*, 1269–1278; c) D. Bochicchio, M. Salvalaglio, G. M. Pavan, *Nat. Commun.* **2017**, *8*, 147; d) M. J. Webber, E. A. Appel, E. W. Meijer, R. Langer, *Nat. Mater.* **2016**, *15*, 13–26; e) J. Guo, B. L. Tardy, A. J. Christofferson, Y. Dai, J. J. Richardson, W. Zhu, M. Hu, Y. Ju, J. Cui, R. R. Dagastine, I. Yarovsky, F. Caruso, *Nat. Nanotechnol.* **2016**, *11*, 1105–1111; f) J.-F. Lutz, J.-M. Lehn, E. W. Meijer, K. Matyjaszewski, *Nat. Rev. Mater.* **2016**, *1*, 16024; g) H. Wang, Y. Li, N. Li, A. Filosa, X. Li, *Nat. Rev. Mater.* **2021**, *6*, 145–167; h) J. D. Rimer, *Proc. Natl. Acad. Sci. U. S. A.* **2020**, *117*, 3360–3362; i) J. J. Richardson, M. Björnmalm, F. Caruso, *Science* **2015**, *348*, aaa2491; j) A. Glotov, A. Stavitskaya, Y. Chudakov, E. Ivanov, W. Huang, V. Vinokurov, A. Zolotukhina, A. Maximov, E. Karakhanov, Y. Lvov, *Bull. Chem. Soc. Jpn.* **2019**, *92*, 61–69; k) Q. Wang, D. Astruc, *Chem. Rev.* **2020**, *120*, 1438–1511; l) R.-B. Lin, L. Li, H.-L. Zhou, H. Wu, C. He, S. Li, R. Krishna, J. Li, W. Zhou, B. Chen, *Nat. Mater.* **2018**, *17*, 1228–1133; m) H. Wang, Z. Zeng, P. Xu, L. Li, G. Zeng, R. Xiao, Z. Tang, D. Huang, L. Tang, C. Lai, D. Jiang, Y. Liu, H. Yi, L. Qin, S. Ye, X. Ren, W. Tang, *Chem. Soc. Rev.* **2019**, *48*, 488–516; n) H. Wang, H. Wang, Z. Wang, L. Tang, G. Zeng, P. Xu, M. Chen, T. Xiong, C. Zhou, X. Li, D. Huang, Y. Zhu, Z. Wang, J. Tang, *Chem. Soc. Rev.* **2020**, *49*, 4135–4165.

[7] a) L. Dong, Z. A. Gao, N. Lin, *Prog. Surf. Sci.* **2016**, *91*, 101–135; b) J. Zhou, Z. Lin, M. Penna, S. Pan, Y. Ju, S. Li, Y. Han, J. Chen, G. Lin, J. J. Richardson, I. Yarovsky, F. Caruso, *Nat. Commun.* **2020**, *11*, 4804; c) K. Aratsu, R. Takeya, B. R. Pauw, M. J. Hollamby, Y. Kitamoto, N. Shimizu, H. Takagi, R. Haruki, S. I. Adachi, S. Yagai, *Nat. Commun.* **2020**, *11*, 1623; d) C. G. Pappas, R. Shafi, I. R. Sasselli, H. Siccardi, T. Wang, V. Narang, R. Abzalimov, N. Wijerathne, R. V. Ulijn, *Nat. Nanotechnol.* **2016**, *11*, 960–967; e) T. Kamperman, M. Koerselman, C. Kelder, J. Hendriks, J. F. Crispim, X. de Peuter, P. J. Dijkstra, M. Karperien, J. Leijten, *Nat. Commun.* **2019**, *10*, 4347; f) L. Li, G. Zhang, Z. Su, *Angew. Chem. Int. Ed.* **2016**, *55*, 9093–9096; *Angew. Chem.* **2016**, *128*, 9239–9243.

[8] a) M. J. Sever, J. J. Wilker, *Dalton Trans.* **2004**, *33*, 1061–1072; b) Q. Xu, M. Xu, C. Y. Lin, Q. Zhao, R. Zhang, X. Dong, Y. Zhang, S. Tian, Y. Tian, Z. Xia, *Adv. Sci.* **2019**, *6*, 1902043; c) W. Zhu, G. Xiang, J. Shang, J. Guo, B. Motevalli, P. Durfee, J. O. Agola, E. N. Coker, C. J. Brinker, *Adv. Funct. Mater.* **2018**, *28*, 1705274; d) J. Wei, G. Wang, F. Chen, M. Bai, Y. Liang, H. Wang, D. Zhao, Y. Zhao, *Angew. Chem. Int. Ed.* **2018**, *57*, 9838–9843; *Angew. Chem.* **2018**, *130*, 9986–9991; e) P. Harvey, A. Nonat, C. Platas-Iglesias, L. S. Natrajan, L. J. Charbonniere, *Angew. Chem. Int. Ed.* **2018**, *57*, 9921–9924; *Angew. Chem.* **2018**, *130*, 10069–10072.

[9] a) S. Pan, R. Guo, N. Bertleff-Zieschang, S. Li, Q. A. Besford, Q.-Z. Zhong, G. Yun, Y. Zhang, F. Cavalieri, Y. Ju, E. Goudeli, J. J. Richardson, F. Caruso, *Angew. Chem. Int. Ed.* **2020**, *59*, 275–280; *Angew. Chem.* **2020**, *132*, 281–286; b) H. Ejima, J. J. Richardson, F. Caruso, *Nano Today* **2017**, *12*, 136–148; c) N. Holten-Andersen, M. J. Harrington, H. Birkedal, B. P. Lee, P. B. Messersmith, K. Y. Lee, J. H. Waite, *Proc. Natl. Acad. Sci. U. S. A.* **2011**, *108*, 2651–2655.

[10] a) J. Yang, M. A. Cohen Stuart, M. Kamperman, *Chem. Soc. Rev.* **2014**, *43*, 8271–8298; b) S. Hong, Y. Wang, S. Y. Park, H. Lee, *Sci. Adv.* **2018**, *4*, eaat7457.

[11] a) Y. Kim, R. J. Macfarlane, M. R. Jones, C. A. Mirkin, *Science* **2016**, *351*, 579–582; b) H. Sun, C. P. Kabb, M. B. Sims, B. S. Sumerlin, *Prog. Polym. Sci.* **2019**, *89*, 61–75.

[12] a) R. D. McGillicuddy, S. Thapa, M. B. Wenny, M. I. Gonzalez, J. A. Mason, *J. Am. Chem. Soc.* **2020**, *142*, 19170–19180; b) J. Rodriguez, I. Beurroies, M. V. Coulet, P. Fabry, T. Devic, C. Serre, R. Denoyel, P. L. Llewellyn, *Dalton Trans.* **2016**, *45*, 4274–4282.

[13] J. Wang, Y. Cui, D. Wang, *Adv. Mater.* **2019**, *31*, e1801993.

[14] X. Wang, J. Feng, Y. Bai, Q. Zhang, Y. Yin, *Chem. Rev.* **2016**, *116*, 10983–11060.

[15] M. C. Biesinger, B. P. Payne, A. P. Grosvenor, L. W. M. Lau, A. R. Gerson, R. S. C. Smart, *Appl. Surf. Sci.* **2011**, *257*, 2717–2730.

[16] M. A. Rahim, K. Kempe, M. Müllner, H. Ejima, Y. Ju, M. P. van Koeverden, T. Suma, J. A. Braunger, M. G. Leeming, B. F. Abrahams, F. Caruso, *Chem. Mater.* **2015**, *27*, 5825–5832.

[17] a) P. Harris, *C* **2018**, *4*, 4; b) Y. Eom, S. M. Son, Y. E. Kim, J.-E. Lee, S.-H. Hwang, H. G. Chae, *Carbon* **2019**, *150*, 142–152.

[18] a) H. W. Liang, Q. F. Guan, L. F. Chen, Z. Zhu, W. J. Zhang, S. H. Yu, *Angew. Chem. Int. Ed.* **2012**, *51*, 5101–5105; *Angew. Chem.* **2012**, *124*, 5191–5195; b) Y. Lee, K. Jun, K. Lee, Y. C. Seo, C. Jeong, M. Kim, I. K. Oh, H. Lee, *Angew. Chem. Int. Ed.* **2020**, *59*, 3864–3870; *Angew. Chem.* **2020**, *132*, 3892–3898; c) Z.-Y. Wu, S.-L. Xu, Q.-Q. Yan, Z.-Q. Chen, Y.-W. Ding, C. Li, H.-W. Liang, S.-H. Yu, *Sci. Adv.* **2018**, *4*, eaat0788.

[19] a) T. K. Kim, K. J. Lee, J. Y. Cheon, J. H. Lee, S. H. Joo, H. R. Moon, *J. Am. Chem. Soc.* **2013**, *135*, 8940–8946; b) J. Rodríguez-Hernández, E. Bormashenko, *Breath Figures*, Springer Nature, Switzerland AG, **2020**, pp. 149–168; c) G. Zhang, B. Li, Y. Zhou, X. Chen, B. Li, Z. Y. Lu, L. Wu, *Nat. Commun.* **2020**, *11*, 425.

[20] a) Y. Lu, S. Sathasivam, J. Song, C. R. Crick, C. J. Carmalt, I. P. Parkin, *Science* **2015**, *347*, 1132–1135; b) W. Xu, H. Zheng, Y. Liu, X. Zhou, C. Zhang, Y. Song, X. Deng, M. Leung, Z. Yang, R. X. Xu, Z. L. Wang, X. C. Zeng, Z. Wang, *Nature* **2020**, *578*, 392–396; c) G.-T. Yun, W.-B. Jung, M. S. Oh, G. M. Jang, J. Baek, N. I. Kim, S. G. Im, H.-T. Jung, *Sci. Adv.* **2018**, *4*, eaat4978.

[21] H. Arora, P. Du, K. W. Tan, J. K. Hyun, J. Grazul, H. L. Xin, D. A. Muller, M. O. Thompson, U. Wiesner, *Science* **2010**, *330*, 214–219.

[22] a) N. T. Padmanabhan, H. John, *J. Environ. Chem. Eng.* **2020**, *8*, 104211; b) G. Kwon, D. Panchanathan, S. R. Mahmoudi, M. A. Gondal, G. H. McKinley, K. K. Varanasi, *Nat. Commun.* **2017**, *8*, 14968; c) R. Wang, K. Hashimoto, A. Fujishima, M. Chikuni, E. Kojima, A. Kitamura, M. Shimohigoshi, T. Watanabe, *Nature* **1997**, *388*, 431–432.

[23] L. Zhang, R. Dillert, D. Bahnemann, M. Vormoor, *Energy Environ. Sci.* **2012**, *5*, 7491–7507.

[24] L. Pan, M. Ai, C. Huang, L. Yin, X. Liu, R. Zhang, S. Wang, Z. Jiang, X. Zhang, J. J. Zou, W. Mi, *Nat. Commun.* **2020**, *11*, 418.

[25] S. Pujals, N. Feiner-Gracia, P. Delcanale, I. Voets, L. Albertazzi, *Nat. Rev. Chem.* **2019**, *3*, 68–84.

[26] Y. Sun, N. Liu, Y. Cui, *Nat. Energy* **2016**, *1*, 16071.
[27] A. Alsbaiee, B. J. Smith, L. Xiao, Y. Ling, D. E. Helbling, W. R. Dichtel, *Nature* **2016**, *529*, 190–194.
[28] Y. Lu, A. A. Aimetti, R. Langer, Z. Gu, *Nat. Rev. Mater.* **2016**, *2*, 16075.
[29] G. P. Maier, M. V. Rapp, J. H. Waite, J. N. Israelachvili, A. Butler, *Science* **2015**, *349*, 628–632.

Entry for the Table of Contents

Insert graphic for Table of Contents here.

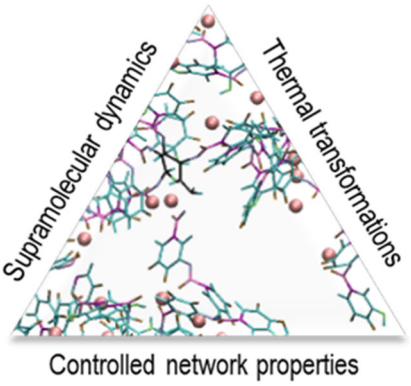

Supramolecular metal–phenolic networks, consisting of metal ions coordinated with phenolic motifs, can undergo selective thermodynamic transformations into nanoporous structures, including metal–carbon networks and metal–oxide networks, with tunable network organization and surface wettability.